ELSEVIER

Site epimerization in *ansa*-zirconocene polymerization catalysts

Martin Graf [a], Klaus Angermund [a], Gerhard Fink [a], Walter Thiel [a,*], Vidar R. Jensen [b,*]

[a] *Max-Planck-Institut für Kohlenforschung, Kaiser-Wilhelm-Platz 1, D-45470 Mülheim an der Ruhr, Germany*
[b] *Department of Chemistry, University of Bergen, Allegaten 41, N-5007 Bergen, Norway*

Abstract

Metallocene alkyl cations for polymerization of olefins possess two active sites involved in migratory insertion. Site epimerization, with an inversion at the metal atom, is considered to be one of the major causes for break-down of the alternating propagation model, resulting in stereoerrors whenever the two catalytic sites have substantially different enantioface selectivities. Density functional theory has been used to determine the intrinsic reaction coordinate that connects the optimized minima and transition states of inversion in the parent *ansa*-zirconocene $[\{H_2C(Cp)_2\}Zr-Pr]^+$ (Pr = *n*-propyl). These calculations yield a three-step reaction path for site epimerization. Starting from the pyramidal β-agostic complex, an activated rotation around the Zr–Pr bond first produces an α-agostic conformation. Continued rotation leads to an equivalent second α-agostic intermediate and then finally to the inverted β-agostic complex. The second step is rate-determining and proceeds through a planar three-coordinate transition state. In the case of $[\{H_2C(Cp)_2\}Zr-{}^iBu]^+$ (${}^iBu$ = *iso*-butyl), the situation is more complicated, because there are several interconvertible α-, β- and γ-agostic intermediates, but the rate-limiting step is again an inversion process connecting two different α-agostic conformers with the alkyl group on opposite enantiosides. For both *ansa*-zirconocene catalysts, the computed free-energy barriers for epimerization are around 11–12 kcal/mol and almost independent of temperature, while those for insertion increase with temperature due to the entropic cost of association. According to the computational results for the isolated catalysts, insertion remains favored over epimerization for the experimentally relevant temperature range in the *n*-propyl case, whereas both processes are competitive in the *iso*-butyl case. Inclusion of bulk solvent effects by a continuum solvation model does not affect the results much, while explicit consideration of a coordinating counterion causes larger changes. The present model calculations on the role of site epimerization should thus be most relevant for propene polymerization with non-coordinating counterions.
© 2006 Elsevier B.V. All rights reserved.

Keywords: Zirconocenes; Olefin polymerization; Density functional theory

1. Introduction

Metallocene catalysts for polymerization of propene are capable of producing polypropenes with a wide variety of structures and properties [1,2]. This flexibility arises from the fact that each metallocene catalyst possesses two distinct active sites, in the following termed A and B (cf. Scheme 1), which can bind and insert the propene monomer. These two sites originate from positions occupied by

σ-ligands (typically halides or alkyl groups) in the tetrahedral precursor complexes, as for example in the simple metallocene complex Cp_2ZrCl_2 (Cp = cyclopentadienyl anion). Taking the active species to be the corresponding alkylated cation, $[Cp_2ZrR]^+$ [3,4], the propene molecule coordinates to one of these sites in the pre-insertion π complex, $[Cp_2ZrR(C_3H_6)]^+$, while the growing polymer chain (R) occupies the other. During insertion of the olefin into the metal–polymeryl bond the latter is transferred to the position previously occupied by the olefin, i.e., the polymer chain migrates from one coordination site to the other during olefin insertion, as originally postulated by Cossee and Arlman [5–7]. Thus, during normal propagation the position of the polymer chain alternates between the two sites,

---

* Corresponding authors. Tel.: +49 208 306 2150; fax: +49 208 306 2996 (W. Thiel), Tel.: +47 55583489; fax: +47 55589490 (V.R. Jensen).
  E-mail addresses: thiel@mpi-muelheim.mpg.de (W. Thiel), Vidar.Jensen@kj.uib.no (V.R. Jensen).
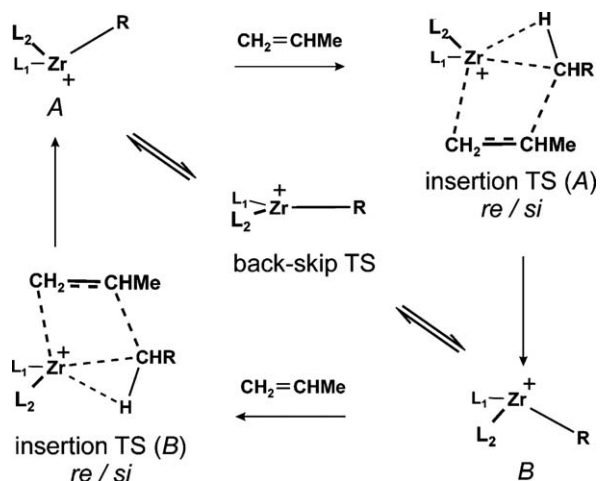
Scheme 1. Intermediate chain migration and propagation cycle of propene polymerization for a generic, three-coordinate, alkyl zirconocene cation.

Scheme 2. Modified Fischer-projection of an isolated *m*-diad stereodefect in syndiotactic propene.

the chiral induction of which may determine the polymer microstructure. If the enantioface selectivity is identical for the two sites (homotopic sites), the polymer produced is isotactic whereas syndiotactic polymer results if there is a preference for opposite propene enantiofaces, termed *re* and *si* [8], exerted by the two sites (enantiotopic sites). For stereorigid catalysts with sites exerting a clear chiral induction, qualitative prediction of the polymer microstructure may be relatively straightforward and based on symmetry considerations [9], and relatively simple, statistical models may, in fact, allow for a near-quantitative prediction of the polypropene microstructure [10,11].

However, these predictions so far require that the reaction proceeds by propagation cycles involving strict alternation between insertions into A and B (Scheme 1), respectively, and any competing reactions with rates comparable to those of alternating propagation must be taken into account. The conceptually simplest cause for breakdown of the alternating propagation model may be termed "site epimerization" (or "back-skip", or "intermediate chain migration"): the growing chain changes position (site) without inserting a monomer, which results in two consecutive insertions at the same active site (see Scheme 1, equilibrium between alkene-free complexes A and B).

Chain migration without insertion does not influence the polymer structure from a catalyst with homotopic sites, but is presumably the major cause for stereoerrors whenever the two catalytic sites have substantially different enantioface selectivities. For example, in polymerizations using the syndiospecific catalyst Me$_2$C(CpFlu)ZrCl$_2$ (Flu = fluorenyl anion), these errors manifest themselves as isolated *m*-diads (or *rrmr* pentads) in a polymer structure otherwise dominated by *rrrr* pentads (Scheme 2). At 10 °C the polymer produced has a close to perfect syndiotactic structure, with 93% intensity for the *rrrr* pentad [12]. At 70 °C the corresponding intensity is down to 59%, a reduction which is much more dramatic than that predicted by a model which only includes alternating propagation and does not
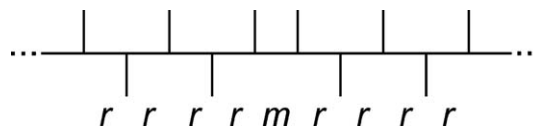
account for any competing reactions [10,12]. Similar large temperature dependencies can be observed for the related, C_1-symmetric class of substituted catalysts, Me$_2$C(3-R-CpFlu)ZrCl$_2$ [10]. Development of computational schemes for accurate prediction of polymer microstructure is particularly important for C_1-symmetric catalysts for which the symmetry rules [9] do not apply and where it may be difficult to decide about enantioface selectivity on the basis of visual inspection alone. Insight into the chain back-skip process is needed for further progress in this area.

The dominance of alternating propagation in polymerization suggests that the barrier to back-skip of the chain normally is higher than that of propagation, i.e., that there is a significant barrier to inversion at the metal atom in the catalyst complexes. Given the complete set of pentads, the corresponding probability of back-skip can be calculated [13], thus offering an indirect measure of the corresponding barrier. More direct estimates have been obtained by Marks et al. [14–17] using dynamic NMR techniques in the study of symmetry-inverting cation–anion separation and reorganization processes involving [(1,2-Me$_2$Cp)$_2$ZrMe]$^+$ and various borate anions. Similar techniques have been used to measure the barrier to site epimerization also for cationic zirconocene complexes with pendant olefins [18,19]. These experimental studies provide a direct proof of the predicted hindrance to inversion at the metal.

Except for a few cases (mostly represented by scandium complexes) the preference for a pyramidal over a planar (trigonal) geometry has been confirmed in quantum-chemical calculations on various three-coordinate transition metal d^0 complexes [20–26]. Based on molecular mechanics (MM) calculations, Castonguay and Rappé [23] reported inversion barriers for a couple of zirconocenes, with and without the presence of a counterion, whereas Guerra et al. [27] used MM energy differences between pre-insertion propene complexes of various metallocenes as a measure of the probability of back-skip. Margl et al. [25] studied the bending potentials of various transition metal alkyls using density functional theory (DFT). The above-mentioned computational studies are relevant because the barrier to inversion at the metal center in a polymerization catalyst, i.e., the barrier of the back-skip process, can be expected to correlate with the preference that a simple three-coordinate transition metal fragment, X$_2$MCH$_3^+$, shows for a pyramidal over a planar geometry. However, a realistic description of intermediate chain migration in a polymerization catalyst also must take into account the metal–H agostic interactions and the complicated rotations

about M–C and C–C bonds expected to occur during inversion at a metal center bound to a growing polymer chain. In addition, inversion is likely to be affected by the co-catalyst as well as by the solvent which thus ideally should be included in a computational model for accurate description of the back-skip reaction. Apart from a preliminary report from the present work [28], we are aware of only one quantum chemical investigation of the site epimerization process in which a realistic model of the active catalyst cation has been used [29]. Using DFT, Borrelli et al. [29] located transition states for the back-skip reaction in $[Cp_2Ti–Et]^+$, $[Cp_2Zr–Et]^+$, $[\{Me_2Si(Cp_2)\}Zr–Et]^+$, $[\{Me_2Si(Ind_2)\}Zr–Et]^+$ and $[\{Me_2C(CpFlu)\}Zr–Et]^+$. The barriers to back-skip were found to be in the range 9–10 kcal/mol, significantly higher than those reported for group 4 methyl metallocenes and halides [21–24,26]. Borrelli et al. thus concluded that "back-skip barriers for higher alkyls can be substantially larger than for methyls". They did, however, not offer structural information pertaining to the reaction pathway or the optimized transition states of the back-skip reaction.

In contrast to the scarce information available on the back-skip reaction, several investigations of another side reaction, the growing chain-end epimerization, have been reported [30–35]. However, the bulk of the quantum chemical investigations of polymerization catalysts have concentrated on the propagation step, with numerous studies of zirconocene catalyzed olefin polymerization appearing over the years. Most of these studies have been based on an alkyl cation [3,4] as the active species, see, e.g., Refs. [10,11,22,24,29–71]. The properties of the catalyst are also governed by the co-catalyst and the degree of cation–anion association [17,72,73] and the role of the co-catalyst anion has been the subject of a series of theoretical investigations that started with the use of overall neutral models of classical titanium chloride/aluminum alkyl catalysts [74–77]. The catalyst–co-catalyst interaction in metallocene catalysts for olefin polymerization has been studied particularly intensively in recent years, see, e.g., Refs. [38,51,78–102].

The lack of information about the intermediate chain migration reaction, in particular the structural changes involved during the "flipping" of the alkyl chain from one site to the other in the metal complex has prompted us to embark on a computational investigation of this process as a competing reaction to propagation. To this end, we have performed a detailed mechanistic study of a simple model system at the DFT level. Here, we report for the first time a complete reaction path (resting state to resting state), based on intrinsic reaction coordinate (IRC) calculations, for back-skip of the chain from one site to the other (A to B in Scheme 1). The reaction path has been obtained for the smallest possible *ansa*-zirconocene cation, $[\{H_2C(Cp)_2\}Zr–Pr]^+$ (Pr = *n*-propyl), which implies a model of the growing polymer chain resulting from insertion of one ethylene molecule into a Zr–Me bond in the catalyst. Back-skip of the polymer chain affects the microstructure of the polymer resulting from propene poly-

merization using catalysts with enantiotopic or diastereotopic sites and we have thus also located minima and transition states pertaining to back-skip using a model of the growing chain resulting from insertion of one propene molecule into a Zr–Me bond in the catalyst, i.e., $[\{H_2C(Cp)_2\}Zr–^iBu]^+$ (^iBu = isobutyl). In addition, for the latter system we have performed a series of calculations with the presence of a counterion, $[(C_6F_5)_3B(CH_3)]^-$, and also using the "conductorlike screening model" (COSMO) in order to estimate effects from the co-catalyst and the solvent on the site epimerization process.

2. Computational details

Geometry optimizations were performed using the BPW91 functional as implemented in the GAUSSIAN 98 set of programs [103]. This functional contains the local exchange-correlation potential developed by Vosko et al. [104] augmented with Becke's [105] non-local exchange corrections and Perdew and Wang's [106] non-local correlation corrections. BPW91 has been found to give accurate energy profiles for the monomer insertion step during metal-catalyzed olefin polymerization [107]. Stationary points were optimized and characterized using analytic first and second derivatives of the energy. Minima and transition states (TS) were connected through intrinsic reaction coordinate (IRC) calculations [108,109], and the reaction path was followed in mass-weighted internal coordinates, in steps of 0.1 amu$^{1/2}$ bohr.

Numerical integrations were performed using the "ultrafine" grid of GAUSSIAN 98, consisting of 99 radial shells and 590 angular points per shell, and the GAUSSIAN 98 default values were chosen for the self-consistent-field (SCF) and geometry optimization convergence criteria. Thermochemical values were computed within the harmonic-oscillator, rigid-rotor, and ideal-gas approximations. All stationary points were subjected to single-point (SP) energy calculations. The SP calculations were performed using the "ultrafine" grid described above and the SCF procedure was converged to a RMS change of the density matrix below 10^{-6}.

The following basis set was used for the geometry optimizations (termed DZP): For zirconium, the Hay and Wadt effective core potential (ECP) [110,111] was employed. The ECP replaced the 1s, 2s, 2p, 3s, 3p and 3d electrons whereas the 4s, 4p, 4d, 5s and 5p orbitals of Zr were represented by the Hay and Wadt primitive basis set [111] contracted to [3s,3p,2d]. Carbon and hydrogen atoms were described by standard Dunning and Hay valence double-ζ basis sets [112]. Polarization functions were added to C ($\alpha_d = 0.75$) and H ($\alpha_p = 1.0$) atoms of ethylene and the propyl group.

The SP energy calculations involved an improved basis set (termed TZD2P): C and H atoms of ethylene and the propyl group were described by augmented Dunning triple-ζ sets denoted TZD2P [107] to account for known basis set sensitivities [107] and polarization functions were

included for the five C atoms of the Cp ring ($\alpha_d = 0.75$). Finally, the outermost primitive was split off from each of the contracted 5s, 5p and 4d functions in the Zr valence basis set described above to give a final [4s,4p,3d]-basis set involving 311, 111 and 211 contractions for the 5s, 5p and 4d functions, respectively.

Solvent and counterion effects were studied using the TURBOMOLE program package version 5.71 [113]. These calculations employed the BP86 functional [105,114,115] in combination with the RI approximation [116–118] and utilized DZ basis sets [110–112] (DZP without polarization functions) and analogous convergence criteria and integration grids as before. Bulk solvent effects were treated by the COSMO continuum model [119] as implemented in TURBO-MOLE [120]. The COSMO radii for the atoms were taken from the literature [94]. COSMO geometry optimizations were started from the stationary points obtained in previous gas-phase calculations. Transition states were located using the CHEMSHELL package [121] and the HDLC optimizer [122].

3. Results and discussion

3.1. [{$H_2C(Cp)_2$}Zr–Pr]$^+$ (Pr = n-propyl)

A Zr–alkyl structure featuring a pronounced β-C–H agostic interaction with the metal atom has been established as the undisputed resting state in computational investigations of olefin polymerization using zirconocene catalysts [30,123]. This does not only imply that the β-agostic structures are the most stable among the possible alkene-free conformers, but also that the latter are more stable, in terms of free energy, than the corresponding (alkene)metal–alkyl complexes. For the present model catalyst, [{$H_2C(Cp)_2$}ZrC_3H_7]$^+$, two practically degenerate β-agostic structures have been located and these appear to constitute the resting state for the present catalyst, see Fig. 1. A γ-agostic structure was also located, but this minimum is ca. 3 kcal/mol less stable than the β-agostic structures. Counting the agostic hydrogen atom as the fourth ligand in the coordination sphere of zirconium, the two β-agostic structures may be termed trigonal pyramidal (Fig. 1, left) and tetrahedral (Fig. 1, right), respectively [25]. The interconversion between the two is facile (see

Fig. 1, middle, for the TS) and corresponds to a transition between a planar and pyramidal three-coordinate L$_2$ZrPr fragment. The structures involved may conveniently be characterized by an angle θ ($\theta = 360° - \angle Cp1ZrCp2 - \angle Cp1ZrC\alpha - \angle Cp2ZrC\alpha$), defining the departure from planarity for the three-coordinate fragment, and the (signed) distances, $d\alpha$ (Cα,Cp1ZrCp2) and $d\beta$ (Cβ,Cp1Zr-Cp2), being the shortest distances from the L$_2$Zr-plane to the α- and β-carbon atom, respectively (cf. Table 1). The **1β1**–**1β2** step is accompanied by an increase in θ from 0.1° to 28.2°, thus underlining the departure from planarity. In accordance with the general trend found by Margl et al. [25], the agostic interaction is stronger in the trigonal structure, the corresponding Cβ–Hβ bond being 3 pm longer than in the tetrahedral case.

Next, we assumed that a symmetric path of inversion connects the two equivalent alkene-free resting states (A and B in Scheme 1). We found a locally planar, C_s-symmetric structure (labeled [**1α**–**1α′**]‡ in Fig. 2), with both Cα–Hα bonds lengthened by 1–2 pm due to agostic interaction with the metal, which has only one imaginary frequency corresponding to a symmetry-breaking rotation of the propyl chain (a″). This structure is a likely candidate for the TS of inversion about the metal center, and was therefore used as starting point for IRC calculations to establish the connection to the previously found resting states.

The first section of the path is dominated by a rotation around the Zr–Cα bond resulting in a rapid decrease in energy. This rotation leads to a shift away from a symmetric, weak double-agostic interaction involving both the α-agostic bonds, toward a much stronger agostic interaction involving a single Cα–Hα bond located almost coplanar with the bridging C atom, Zr and Cα. Upon arriving at the minimum (**1α** in Fig. 2), the lengthening of the latter Cα–Hα bond ($\delta R_{ag}(\alpha)$) has reached 5 pm, which indicates an α-agostic interaction not much weaker than the β-agostic interaction in **1β2**. Apart from the rotation of the alkyl chain, the geometric changes are small, and the three primary bonds to the metal atom are still not far from coplanar.

The α-agostic structure (**1α**) features a β-hydrogen atom *anti* to the α-agostic bond, suggesting that a β-agostic bond to the metal could be formed by a reduction in the angle $\angle ZrC\alpha C\beta$. A TS search starting from a structure with a

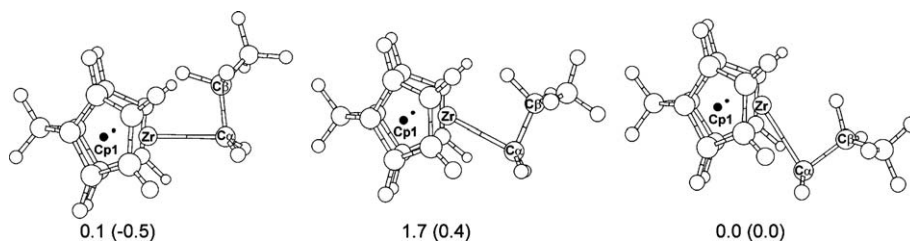0.1 (-0.5)   1.7 (0.4)   0.0 (0.0)

Fig. 1. Counting the agostic hydrogen atom as the fourth ligand coordinated to zirconium, the β-agostic structures may be termed trigonal pyramidal (**1β1**, left) and tetrahedral (**1β2**, right). The TS of interconversion between these two ([**1β1**–**1β2**]‡) is shown in the middle. Free energies, ΔG_{298} (kcal/mol), calculated relative to **1β2**, are given below each structure, with the corresponding enthalpies in parentheses. Cp1 and Cp2 denote the geometric means of the five carbon atom positions in each of the two cyclopentadienyl rings.

Table 1
Geometry parameters for optimized structures of the three-coordinated zirconocene propyl complex, $[\{H_2C(Cp)_2\}Zr–Pr]^+$ (Pr = n-propyl)[a]

|	1β1	[1β1–1β2]‡	1β2	[1β2–1α]‡	1α	[1α–1α′]‡b
Zr–Cp1 (Å)[c]	2.212	2.208	2.210	2.209	2.209	2.214
Zr–Cp2 (Å)[c]	2.213	2.208	2.208	2.213	2.206	2.208
Zr–Cα (Å)	2.244	2.233	2.251	2.211	2.192	2.211
$\delta R_{ag}(\alpha)$ (pm)[d]	0.1	0.1	0.1	1.3	5.0	0.0
$\delta R_{ag}(\beta)$ (pm)[d]	9.0	7.3	6.0	0.5	0.2	0.0
dα (Å)[e]	−0.14	1.06	1.86	0.26	0.47	0.00
dβ (Å)[e]	−1.63	−0.33	0.90	−0.73	0.29	0.00
θ (°)[f]	0.1	8.1	28.2	0.5	1.6	0.0
ϕ (Cp2ZrCαCβ) (°)[g]	90.2	103.3	110.9	56.7	29.1	1.2

[a] See Figs. 1 and 2 for labeling.
[b] Calculation without symmetry constraints.
[c] Cp1 and Cp2 denote the geometric means of the two cyclopentadienyl rings.
[d] $\delta R_{ag}(\alpha) = \max\{C\alpha–H\alpha\} - \min\{C\alpha–H\alpha\}$.
[e] **dα** (Cα,Cp1ZrCp2) and **dβ** (Cβ,Cp1ZrCp2) give the shortest, signed distance from the L_2Zr-plane to the α- and β-carbon atom, respectively.
[f] $\theta = 360° - \angle Cp1ZrCp2 - \angle Cp1ZrC\alpha - \angle Cp2ZrC\alpha$.
[g] Dihedral angle.
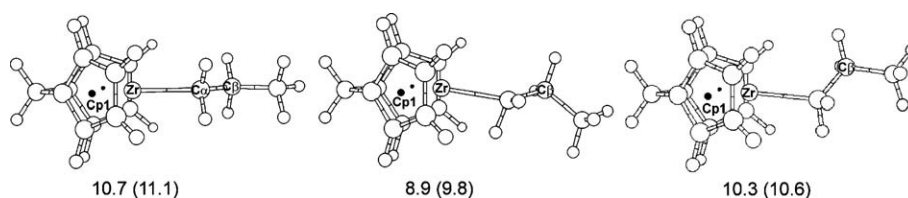
Fig. 2. The TS for inversion about the metal center, [1α–1α′]‡ (left), the α-agostic minimum, 1α (middle), and the TS for the rearrangement between β- and α-agostic conformations, [1β2–1α]‡ (right). The free energy of activation, $\Delta G^{\ddagger}_{298}$ (kcal/mol), calculated relative to 1β2, is given below each structure, with the corresponding enthalpy in parenthesis. Cp1 and Cp2 denote the geometric means of the two cyclopentadienyl rings.

∠ZrCαCβ angle intermediate between that of the α- and β-agostic structures resulted in a transition structure with one imaginary frequency of 77i cm^{-1} ([1β2–1α]‡ in Fig. 2). The imaginary frequency corresponds to a mode involving large changes in the ∠ZrCαCβ angle. IRC calculations in both directions confirm that this TS lies on the path from the α-agostic to a β-agostic structure. Combining the information from all IRC calculations, the C_s-symmetric, back-skip TS ([1α–1α′]‡) is thus connected to the β-agostic resting state 1β2 via the α-agostic minimum 1α and the TS for rearrangement ([1β2–1α]‡). The corresponding structures from [1α–1α′]‡ to the inverted β-agostic resting state can be generated by reflection which then completes the reaction pathway of the site epimerization process. The energy and important geometric variables are presented in Fig. 3 as functions of the path variable, s, from the first β-agostic resting state to the corresponding inverted β-agostic resting state.

The back-skip process starts in the tetrahedral structure 1β2 by movement of the propyl group to approach coplanarity for the L_2ZrCα skeleton along with rotation around the Zr–Cα bond to position an α-H atom close to the plane defined by the bridging C atom, Zr and Cα. During the first phase of the reaction, the β-agostic interaction is kept intact and the energy is increasing only slowly (Fig. 3). At a path coordinate in excess of ca. 0.12, the strength of the β-agostic bond can no longer be maintained, resulting

in a steep increase in energy. In the TS region, the reaction coordinate starts to be dominated by a reduction of the angle ∠ZrCαHα, and reaches the first TS during a phase of simultaneous formation and rupture of the Zr–Hα and Zr–Hβ agostic bonds, respectively (Fig. 3, middle), leading to the α-agostic structure, 1α. As shown by the small values for θ (<2°, Fig. 3, lower part) the complex appears to be essentially planar in the α-agostic region. The signed distance **dα** is a more sensitive measure of departure from planarity: it shows that the L_2ZrCα skeleton is close to planar near the transition states [1β2–1α]‡ and [1α–1α′]‡, but somewhat bent near the α-agostic minimum. In the back-skip TS the β-carbon atom is coplanar with L_2ZrCα (**dβ** = 0, Fig. 3, lower part) as a result of rotation around the Zr–Cα bond (cf. the variation of ϕ (torsion angle ∠Cp2ZrCαCβ), Fig. 3, lower part). This rotation, in turn, ensures a shift of the Zr–Hα agostic bond between the two α-hydrogen atoms (cf. Fig. 3, middle part).

The unimolecular site epimerization reaction requires ca. 11 kcal/mol activation and is as expected little affected by entropy, the free energy of activation being a mere 0.4 kcal/mol lower than the corresponding enthalpy at 298 K (Fig. 2). For comparison, we have also investigated the transition states of ethylene insertion into the Zr–Cα bond and the corresponding pre-insertion Zr–ethylene complexes, see Fig. 4. Both the "frontside" and "backside" approach of ethylene have been considered, depending on
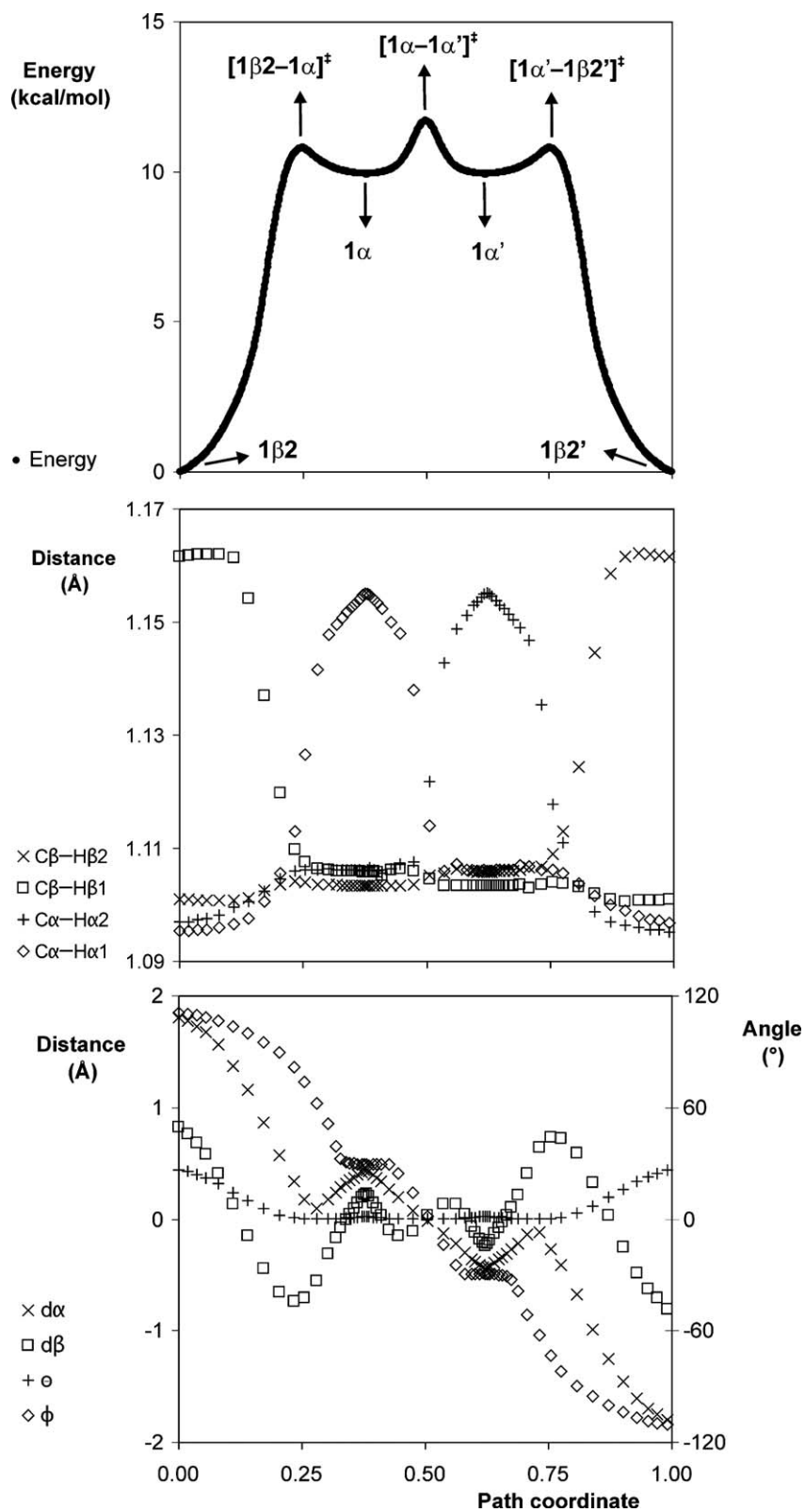
Fig. 3. Energy profile along the reaction pathway of inversion (upper part), and important geometry parameters (lower two parts) from every 32nd point on the IRC. The path coordinate is dimensionless and gives the fraction of the total path length, $s = 94.892$ amu$^{1/2}$ bohr. θ defines the departure from planarity for the three-coordinate fragment ($\theta = 360° - \angle Cp1ZrZp2 - \angle Cp1ZrC\alpha - \angle Cp2ZrC\alpha$), ϕ is the torsion angle $\angle Cp2ZrC\alpha C\beta$, **d$\alpha$** (C$\alpha$,Cp1ZrCp2) and **d$\beta$** (C$\beta$,Cp1ZrCp2) give the shortest, signed distance from the L$_2$Zr-plane to the α- and β-carbon atom, respectively. The energies were obtained using the DZP basis.
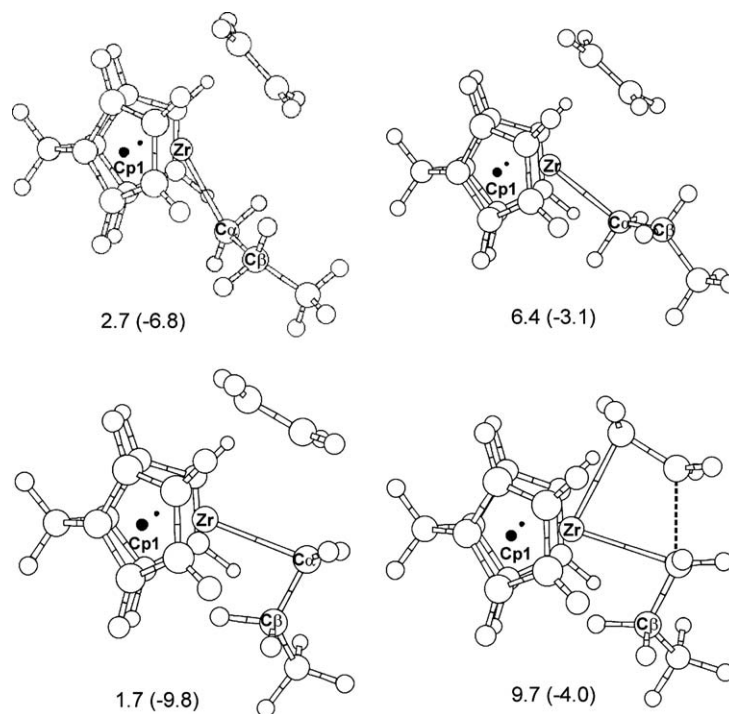
Fig. 4. Optimized pre-insertion π complex, **1Fβ** (left), and TS, [**1Fβ–2γ**]‡ (right), of frontside ethylene insertion (upper part), and the corresponding stationary points, **1Bβ** and [**1Bβ–2δ**]‡, pertaining to backside insertion (lower part). Free energies, ΔG_{298} (kcal/mol), calculated relative to **1β2**, are given below each structure, with the corresponding enthalpies in parentheses.

whether complex formation takes place *syn* or *anti* to the existing β-agostic bond. Consistent with previous results [54,123], frontside insertion is favored over backside insertion (free-energy barriers of 6.4 and 9.7 kcal/mol relative to the resting state, respectively) so that the latter reaction channel can be disregarded in comparison with the back-skip process, which has a computed free-energy barrier of 10.7 kcal/mol (Fig. 2). Thus, judged from the presently calculated energies, insertion is significantly more facile than site epimerization. However, a quantitative comparison of the two barriers is difficult due to the different nature of the two transition states. A fair comparison of the free energy of the two transition states would, among other, require that accurate estimates of the real entropic cost of binding the olefin to the catalyst complex in solution could be obtained.

Even if a detailed comparison of the free energy of the two transition states cannot be performed at present, it is still clear, however, that there is a significant entropic penalty associated with monomer coordination and insertion (e.g., calculated to be 9.5 kcal/mol at 298 K for frontside insertion in our small gas-phase model system, see Fig. 4). On the other hand, the intramolecular site epimerization is not affected much by entropy (small entropic gain of 0.4 kcal/mol at 298 K, see Fig. 2). As a consequence, an increase in temperature will shift the balance between insertion and back-skip processes in favor of the latter, which thus is the main factor behind the experimental observation that site epimerization generally becomes more important at higher temperatures [2,10,12].

3.2. $[H_2C(Cp)_2Zr{-}^iBu]^+$ (^iBu = iso-butyl)

We now turn to the *ansa*-zirconocene cation [{H$_2$C-(Cp)$_2$}Zr–^{i}Bu]$^+$ which provides a model of the growing chain resulting from insertion of one propene molecule into the Zr–Me bond of the initial catalyst. Replacing *n*-propyl by *iso*-butyl gives rise to additional complexity since there are now more possible conformers for the three agostic species (α, β, and γ). Fig. 5 indicates the agostic minima considered and the interconversions that have been studied. Table 2 summarizes the relative energies for the relevant conformers and transition states.

The optimized geometries for the various conformers and transition states in [{H$_2$C(Cp)$_2$}Zr–^{i}Bu]$^+$ generally closely resemble those in [{H$_2$C(Cp)$_2$}Zr–^{n}Pr]$^+$, both with regard to qualitative features and quantitative trends, and they will therefore not be presented here in view of the detailed discussion of structural issues for the parent system in the preceding section. We shall instead focus on the energetics of the [{H$_2$C(Cp)$_2$}Zr–^{i}Bu]$^+$ system. Unless noted otherwise, we shall refer to the computed free enthalpies ΔG at 298 K in the following (Table 2).

It is obvious that the two β-agostic conformers are almost isoenergetic and easily interconverted, with a barrier of only 1.4 kcal/mol. The γ-agostic conformer which is the primary product of insertion [30,123] is only slightly higher in energy (2.2 kcal/mol) and can also easily rearrange to the β-agostic resting state (via a TS at 4.3 kcal/mol). The three α-agostic conformers are less stable (8.2–10.3 kcal/mol above the resting state). They can be
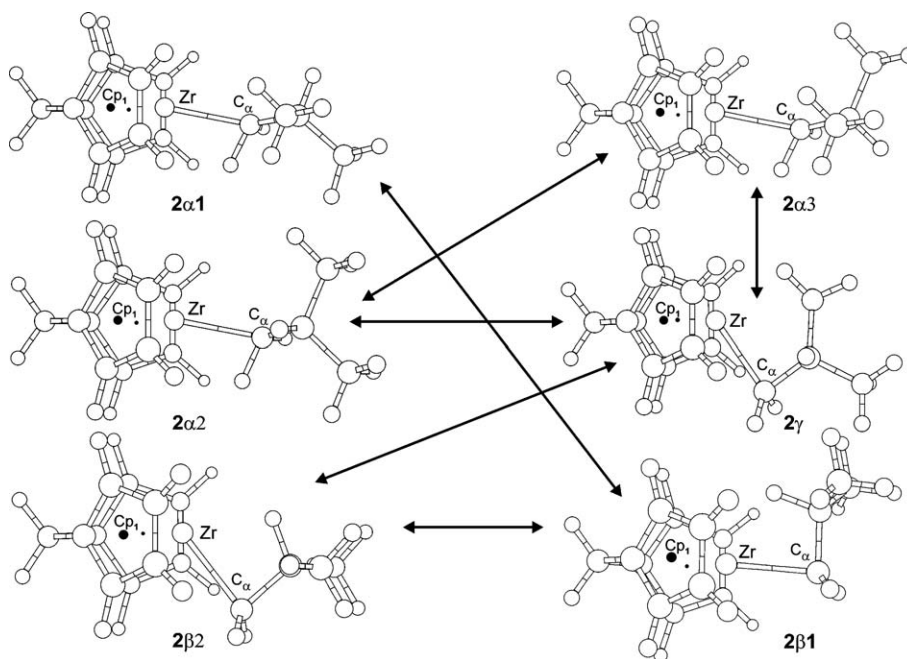
Fig. 5. Agostic conformers in $[\{H_2C(Cp)_2\}Zr-{}^iBu]^+$. **2β1** and **2β2** denote the trigonal-pyramidal and tetrahedral β-agostic minima of the resting state, respectively. **2α1**, **2α2**, and **2α3** are α-agostic conformers, with the C_β–H bond being anti, gauche(+), and gauche(−) with respect to Zr–C_α–C_β–H. **2γ** is the initially formed γ-agostic species. Arrows indicate the interconversions that have been investigated.

Table 2
Enthalpies ΔH and free enthalpies ΔG at 298 K (kcal/mol) relative to the tetrahedral β-agostic resting state

Species[a]	ΔH	ΔG	Species[a]	ΔH	ΔG
2α1	11.5	10.3	TS [**2β1–2β2**]‡	0.2	1.4
2α2	9.6	8.2	TS [**2β1–2α1**]‡	12.2	11.6
2α3	11.4	10.2	TS [**2α1–2α1′**]‡	12.8	13.2
2β1	0.03	0.2	TS [**2α1–2α3′**]‡	12.4	11.8
2β2	0.0	0.0	TS [**2α2–2α3′**]‡	12.8	13.2
2γ	1.8	2.2	TS [**2α3–2α2′**]‡	13.2	13.0
TS [**2γ–2α2**]‡	9.8	9.5	TS **2Fβ** (insertion)	2.1	11.3
TS [**2γ–2α3**]‡	12.2	11.8	TS **2Bβ** (insertion)	−0.6	13.5
TS [**2γ–2β2**]‡	2.8	4.3			

[a] See Fig. 5 for notation. A prime denotes mirror-image structures in which the *iso*-butyl group has moved to the other side (after back-skip inversion). TS **2Fβ** and TS **2Bβ** refer to the transition states of frontside and backside propene insertion into $[\{H_2C(Cp)_2\}Zr-{}^iBu]^+$, respectively.

accessed from the **2γ** and **2β1** conformers through transition states lying between 9.5 and 11.6 kcal/mol. These processes lead to α-agostic structures where the *iso*-butyl remains on the same side (no inversion yet). The actual back-skip occurs in the conversion of α-agostic species to α′-agostic mirror-image species via transition states between 11.6 and 13.2 kcal/mol. These α′-type conformers can then rearrange to the β′- and α′-type conformers, all of them with the *iso*-butyl group on the other side. The primed species are equivalent to the unprimed ones (mirror images) and hence there is no need to discuss them or their interconversions again.

Given the conformational complexity of $[\{H_2C(Cp)_2\}$-$Zr-{}^iBu]^+$, several pathways for the overall back-skip process can be constructed starting from the initially available

γ-agostic conformer. The shortest sequence is **2γ → 2α2 → 2α3′ → 2γ′**, with the highest transition state at 13.2 kcal/mol. In reality, the γ-and β-agostic conformers will pre-equilibrate before conversion to α-agostic species and back-skip, so a more likely symmetric pathway is **2γ → 2β2 → 2β1 → 2α1 → 2α1′ → 2β1′ → 2β2′ → 2γ′**, which also proceeds via a rate-limiting transition state at 13.2 kcal/mol. However, the unsymmetrical back-skip process **2α1 → 2α3′** (from an anti to a gauche-conformation) is slightly more facile, so that the scenario **2γ → 2β2 → 2β1 → 2α1 → 2α3′ → 2γ′** is actually most favorable, with the highest transition state at 11.8 kcal/mol. The advantage of the unsymmetrical over the symmetrical pathway (1.4 kcal/mol) is not large, but still relevant for an accurate treatment of reaction kinetics.

For the agostic conformers and transition states considered so far, the entropic contributions to the relative free enthalpies are small, and the ΔH and ΔG values are therefore close to each other (Table 2). This is different in the case of the transition states for frontside and backside insertion of propene into $[\{H_2C(Cp)_2\}Zr-{}^iBu]^+$ which show a large entropic penalty mainly due to the loss of six degrees of freedom upon association. The magnitude of this entropic penalty (Table 2) will be overestimated by the present gas-phase treatment that neglects the contributions from desolvation and solvation. Taking the computed gas-phase free enthalpies at face value, the insertion barriers are of similar magnitude as the back-skip barriers. Frontside insertion is slightly favored over backside insertion (barriers of 11.3 and 13.5 kcal/mol, respectively) and competitive with the preferred back-skip path (see above). As already pointed out for the parent system

$[\{H_2C(Cp)_2\}Zr-^nPr]^+$, the free enthalpy of activation should be almost temperature-independent for the intra-molecular back-skip process, but should increase with temperature for intermolecular olefin insertion. Fig. 6 shows the computed temperature dependence of the barriers for $[\{H_2C(Cp)_2\}Zr-^iBu]^+$: as expected, both ΔH curves and the ΔG curve for back-skip are almost horizontal, while the ΔG curve for insertion rises by almost 4 kcal/mol between 273 and 353 K, and actually crosses the ΔG curve for back-skip. This example clearly illustrates how higher temperatures can favor back-skip over inversion, even though it should be emphasized that these gas-phase model results will not accurately reflect the situation in real-life systems with solvent and counterions.

For a rough assessment of non-specific bulk solvent effects, we have carried out COSMO geometry optimizations (see Section 2) on four selected species: the agostic minima **2β1** and **2α1** as well as the transition states **2β1 → 2α1** and **2α1 → 2α1′**. Using toluene as solvent (dielectric constant of 2.38), the COSMO-induced changes in the computed geometries are very small, with a slight tendency to weaken the agostic interactions compared with the gas-phase results (as judged from the relevant bond lengths). In the COSMO treatment, the chosen transition states are stabilized somewhat more than the corresponding minima, with a concomitant lowering of the investigated barriers (see above) by 0.4–0.6 kcal/mol. These COSMO data suggest that our present results are not affected much by a low-dielectric bulk solvent, and one may anticipate that this also holds to some extent for non-coordinating counterions. Specific counterion effects are expected to be strongest for coordinating anions. The interaction between metallocene cations and co-catalyst anions has been the subject of many recent theoretical studies [38,51,78–102]. Borate anions such as $[(C_6F_5)_3B(CH_3)]^-$ are structurally well-defined and especially suitable for experimental and theoretical investigations of the effects

of the co-catalyst anion, see, e.g., Refs. [16,87,89,92,94,-97]. To check the influence of this typical anion on our results, we have added it to **2α3** and **2β2**, placing it in similar positions as in the published work by Nifant'ev et al. [92], and performed geometry optimizations on the resulting catalyst-counterion complexes (see Figs. S1–S4 in the Supplementary Information).

Introducing the counterion into **2α3** backside to the α-agostic interaction leads to a complex in which $[(C_6F_5)B_3(CH_3)]^-$ is coordinated through the three hydrogen atoms of the methyl group, forming weak agostic interactions. The *iso*-butyl group is pushed into a tetrahedral position, with a change in the angle $C_{bridge}ZrC_\alpha$ from 167.3° to 115.5° and a weakening of the α-agostic interaction that is reflected in a shortening of the $C_\alpha-H_\alpha$ bond by 0.03 Å and an increase of the $Zr-H_\alpha$ distance by 0.23 Å. When the counterion approaches **2α3** frontside to the α-agostic interaction, the coordination of $[(C_6F_5)_3B(CH_3)]^-$ causes the C_α atom, and hence the *iso*-butyl group, to move to the other enantioside of the catalyst. The α-agostic interaction is weakened by about the same amount as in the backside attack, judging from the changes in the corresponding geometrical variables (see above). The frontside coordination of the counterion to **2β3** thus induces an inversion at the stereocenter. By contrast, when the counterion approaches **2β2** backside to the β-agostic interaction, there are only small structural changes in **2β2**: the relatively strong β-agostic bond remains essentially intact, and only a rather loose complex is formed. The frontside coordination of the counterion to **2β2** leads to a tighter complex in which the β-agostic interactions are weakened significantly, as can be seen from the decrease in the $C_\beta-H_\beta$ bond length by 0.04 Å and the increase of the $Zr-H_\beta$ distance by 0.22 Å. The preceding results for isolated catalyst–counterion complexes remain essentially unchanged when COSMO geometry optimizations are performed to include bulk solvent effects.
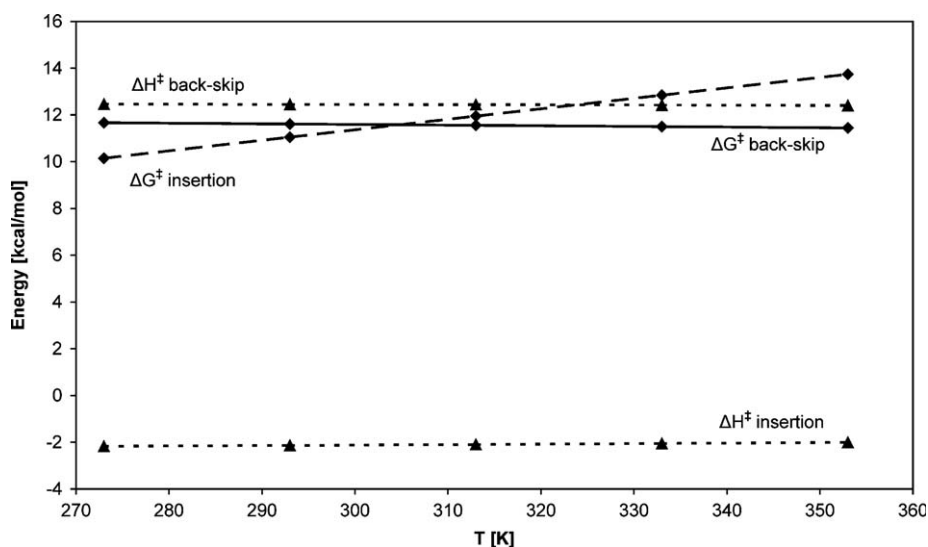

Fig. 6. Temperature dependence of the barriers for back-skip and propene insertion in $[\{H_2C(Cp)_2\}Zr-^iBu]^+$.

These test calculations show that coordination of a counterion such as $[(C_6F_5)_3B(CH_3)]^-$ can cause major structural changes that will generally be different for different agostic conformers of the catalyst. In addition, the relative energies are altered upon complexation: the frontside β-agostic complex is most stable, but the two α-agostic complexes are only about 4 kcal/mol higher in energy; hence, in the case of the frontside complexes, the α-agostic conformer is stabilized by 8 kcal/mol relative to the β-agostic conformer. A similar relative stabilization of the α-agostic conformer by a coordinating anion has been noted previously [92]. One may therefore expect that the presence of coordinating counterions may affect the relative propensity of the back-skip and insertion processes studied presently. In the simplest scenario, one would assume that there is an equilibrium between coordination and decoordination, and that back-skip and insertion will occur only in the free catalyst with one empty coordination site. In this case, the intrinsic reactivity of the free catalyst will govern the preferences for back-skip and insertion, while the overall rate will depend on the equilibrium between coordination and decoordination. On the other hand, one may also envision more complicated mechanisms in which the counterion is directly involved in the back-skip and insertion processes; the study of such mechanisms is beyond the scope of this paper.

4. Conclusions

The present calculations have established the intrinsic reaction path for site epimerization in the parent *ansa*-zirconocene $[\{H_2C(Cp)_2\}Zr-Pr]^+$ which inverts the β-agostic resting state into its mirror image in a three-step rearrangement involving two equivalent α-agostic intermediates. In the case of $[\{H_2C(Cp)_2\}Zr-^iBu]^+$, the situation is more complicated, because there are more interconvertible α-, β- and γ-agostic intermediates, but the rate-limiting step is again an inversion process connecting two different α-agostic conformers. For both these *ansa*-zirconocene catalysts, the computed free-energy barriers for epimerization are around 11–12 kcal/mol and almost independent of temperature. Back-skip processes may cause stereoerrors during polymerization if they can compete with monomer insertion. In the case of $[\{H_2C(Cp)_2\}Zr-Pr]^+$, the frontside insertion of ethylene is more facile (barrier of 6 kcal/mol) implying retention of configuration at zirconium between insertions. For $[\{H_2C(Cp)_2\}Zr-^iBu]^+$, however, the frontside insertion of propene has a similar barrier (11 kcal/mol) as epimerization, so that both processes are expected to be competitive. Due to the entropic cost of association, insertion will become less favorable at higher temperature, implying more stereoerrors because of back-skip.

It should be stressed that these conclusions are based on model DFT calculations on isolated catalysts, without considering solvent and counterion effects. COSMO test calculations show that the inclusion of a low-dielectric solvent does not affect the gas-phase results much. Coordinating counterions can have a more significant influence, however, because the few investigated catalyst-counterion complexes differ considerably from the isolated catalysts both with regard to structure and energetics. The present model calculations on the intrinsic stereochemical importance of back-skip processes should therefore be most relevant for zirconocene-catalyzed propene polymerization with non-coordinating counterions.

Appendix A. Supplementary data

Calculated energies for all reported structures as well as figures showing the optimized structures of the four catalyst-counterion complexes. Supplementary data associated with this article can be found, in the online version, at doi:10.1016/j.jorganchem.2006.01.019.

References

[1] H.H. Brintzinger, D. Fischer, R. Mülhaupt, B. Rieger, R.M. Waymouth, Angew. Chem., Int. Ed. Engl. 34 (1995) 1143.
[2] L. Resconi, L. Cavallo, A. Fait, F. Piemontesi, Chem. Rev. 100 (2000) 1253.
[3] R.F. Jordan, W.E. Dasher, S.F. Echols, J. Am. Chem. Soc. 108 (1986) 1718.
[4] R.F. Jordan, Adv. Organomet. Chem. 32 (1991) 325.
[5] P. Cossee, J. Catal. 3 (1964) 80.
[6] E.J. Arlman, J. Catal. 3 (1964) 89.
[7] E.J. Arlman, P. Cossee, J. Catal. 3 (1964) 99.
[8] K.R. Hanson, J. Am. Chem. Soc. 88 (1966) 2731.
[9] J.A. Ewen, J. Mol. Catal. A-Chem. 128 (1998) 103.
[10] K. Angermund, G. Fink, V.R. Jensen, R. Kleinschmidt, Macromol. Rapid Commun. 21 (2000) 91.
[11] K. Angermund, G. Fink, V.R. Jensen, R. Kleinschmidt, Chem. Rev. 100 (2000) 1457.
[12] Analysis of ^{13}C NMR spectra of the polymer focuses on the chemical shifts of the methyl carbon atoms (which are sensitive to the relative stereochemistry of neighboring monomers), in particular those within sequences of five consecutive monomers (termed a pentad). A given pentad intensity is the ratio of the corresponding pentad integral to the integral sum of all pentad signals observed and is usually given in units of percent.
[13] M. Farina, A. Terragni, Makromol. Chem., Rapid Commun. 14 (1993) 791.
[14] X. Yang, C.L. Stern, T.J. Marks, J. Am. Chem. Soc. 113 (1991) 3623.
[15] P.A. Deck, C.L. Beswick, T.J. Marks, J. Am. Chem. Soc. 120 (1998) 1772.
[16] P.A. Deck, T.J. Marks, J. Am. Chem. Soc. 117 (1995) 6128.
[17] E.Y.X. Chen, T.J. Marks, Chem. Rev. 100 (2000) 1391.
[18] C.P. Casey, D.W. Carpenetti, Organometallics 19 (2000) 3970.
[19] C.G. Brandow, A. Mendiratta, J.E. Bercaw, Organometallics 20 (2001) 4253.
[20] J.W. Lauher, R. Hoffmann, J. Am. Chem. Soc. 98 (1976) 1729.
[21] C.A. Jolly, D.S. Marynick, Inorg. Chem. 28 (1989) 2893.
[22] C.A. Jolly, D.S. Marynick, J. Am. Chem. Soc. 111 (1989) 7968.
[23] L.A. Castonguay, A.K. Rappé, J. Am. Chem. Soc. 114 (1992) 5832.
[24] E.P. Bierwagen, J.E. Bercaw, I.W.A. Goddard, J. Am. Chem. Soc. 116 (1994) 1481.

[25] P. Margl, L.Q. Deng, T. Ziegler, Organometallics 17 (1998) 933.
[26] V.R. Jensen, K.J. Børve, Organometallics 20 (2001) 616.
[27] G. Guerra, L. Cavallo, G. Moscardi, M. Vacatello, P. Corradini, Macromolecules 29 (1996) 4834.
[28] M. Graf, V.R. Jensen, W. Thiel, 1st. Blue Sky Conference on Catalytic Olefin Polymerization, Sorrento, Italy, 2002 (Poster abstract).
[29] M. Borrelli, V. Busico, R. Cipullo, S. Ronca, P.H.M. Budzelaar, Macromolecules 36 (2003) 8171.
[30] V.R. Jensen, D. Koley, M.N. Jagadeesh, W. Thiel, Macromolecules 38 (2005) 10266.
[31] G. Moscardi, L. Resconi, L. Cavallo, Organometallics 20 (2001) 1918.
[32] J.C.W. Lohrenz, M. Bühl, M. Weber, W. Thiel, J. Organomet. Chem. 529 (1999) 11.
[33] K. Thorshaug, J.A. Støvneng, E. Rytter, M. Ystenes, Macromolecules 31 (1998) 7149.
[34] K. Thorshaug, J.A. Støvneng, E. Rytter, M. Ystenes, Macromolecules 31 (1998) 9416 (Erratum).
[35] M.H. Prosenc, H.H. Brintzinger, Organometallics 16 (1997) 3889.
[36] J.L. Eilertsen, J.A. Støvneng, M. Ystenes, E. Rytter, Inorg. Chem. 44 (2005) 4843.
[37] V.R. Jensen, M. Graf, W. Thiel, ChemPhysChem 6 (2005) 1929.
[38] M. Silanes, J.M. Ugalde, Organometallics 24 (2005) 3233.
[39] E. Aitola, M. Surakka, T. Repo, M. Linnolahti, K. Lappalainen, K. Kervinen, M. Klinga, T. Pakkanen, M. Leskela, J. Organomet. Chem. 690 (2005) 773.
[40] S.H. Yang, J. Huh, J.S. Yang, W.H. Jo, Macromolecules 37 (2004) 5741.
[41] E.G. Kim, M.L. Klein, Organometallics 23 (2004) 3319.
[42] P.H.M. Budzelaar, Organometallics 23 (2004) 855.
[43] S.H. Yang, W.H. Jo, S.K. Noh, J. Chem. Phys. 119 (2003) 1824.
[44] H. Wigum, K.A. Solli, J.A. Støvneng, E. Rytter, J. Polym. Sci., Part A: Polym. Chem. 41 (2003) 1622.
[45] S. Martinez, V. Cruz, A. Munoz-Escalona, J. Martinez-Salazar, Polymer 44 (2003) 295.
[46] G. Talarico, A.N.J. Blok, T.K. Wo, L. Cavallo, Organometallics 21 (2002) 4939.
[47] M. Holscher, H. Keul, H. Hocker, Macromolecules 35 (2002) 8194.
[48] M. Borrelli, V. Busico, R. Cipullo, S. Ronca, P.H.M. Budzelaar, Macromolecules 35 (2002) 2835.
[49] R. Blom, O. Swang, R.H. Heyn, Macromol. Chem. Phys. 203 (2002) 381.
[50] M.J. Young, C.C.M. Ma, C. Ting, Russ. J. Coord. Chem. 28 (2002) 25.
[51] K. Vanka, Z.T. Xu, T. Ziegler, Isr. J. Chem. 42 (2002) 403.
[52] G. Lanza, I. Fragala, T.J. Marks, Organometallics 20 (2001) 4006.
[53] M. Linnolahti, T.A. Pakkanen, Macromolecules 33 (2000) 9205.
[54] A.T. Rappé, W.M. Skiff, C.J. Casewit, Chem. Rev. 100 (2000) 1435.
[55] K. Thorshaug, J.A. Støvneng, E. Rytter, Macromolecules 33 (2000) 8136.
[56] I.E. Nifant'ev, L.Y. Ustynyuk, D.N. Laikov, Russ. Chem. Bull. 49 (2000) 1164.
[57] L. Petitjean, D. Pattou, M.F. Ruiz-Lopez, J. Phys. Chem. B 103 (1999) 27.
[58] P.M. Margl, T.K. Woo, P.E. Blöchl, T. Ziegler, J. Am. Chem. Soc. 120 (1998) 2174.
[59] L.Q. Deng, T. Ziegler, T.K. Woo, P. Margl, L.Y. Fan, Organometallics 17 (1998) 3240.
[60] T.K. Woo, P.M. Margl, T. Ziegler, P.E. Blöchl, Organometallics 16 (1997) 3454.
[61] D.G. Musaev, R.D.J. Froese, K. Morokuma, New J. Chem. 21 (1997) 1269.
[62] T.K. Woo, P.M. Margl, J.C.W. Lohrenz, P.E. Blöchl, T. Ziegler, J. Am. Chem. Soc. 118 (1996) 13021.
[63] J.A. Støvneng, E. Rytter, J. Organomet. Chem. 519 (1996) 277.
[64] P. Margl, J.C.W. Lohrenz, T. Ziegler, P.E. Blöchl, J. Am. Chem. Soc. 118 (1996) 4434.
[65] T. Yoshida, N. Koga, K. Morokuma, Organometallics 15 (1996) 766.
[66] T. Yoshida, N. Koga, K. Morokuma, Organometallics 14 (1995) 746.
[67] J.C.W. Lohrenz, T.K. Woo, L.Y. Fan, T. Ziegler, J. Organomet. Chem. 497 (1995) 91.
[68] V.R. Jensen, K.J. Børve, N. Westberg, M. Ystenes, Organometallics 14 (1995) 4349.
[69] T.K. Woo, L. Fan, T. Ziegler, Organometallics 13 (1994) 2252.
[70] H. Kawamura-Kuribayashi, N. Koga, K. Morokuma, J. Am. Chem. Soc. 114 (1992) 8687.
[71] H. Kawamura-Kuribayashi, N. Koga, K. Morokuma, J. Am. Chem. Soc. 114 (1992) 2359.
[72] M.C. Chen, J.A.S. Roberts, T.J. Marks, J. Am. Chem. Soc. 126 (2004) 4605.
[73] L. Jia, X.M. Yang, C.L. Stern, T.J. Marks, Organometallics 16 (1997) 842.
[74] F. Bernardi, A. Bottom, G.P. Miscione, Organometallics 17 (1998) 16.
[75] V.R. Jensen, K.J. Børve, M. Ystenes, J. Am. Chem. Soc. 117 (1995) 4109.
[76] O. Novaro, E. Blaisten-Barojas, E. Clementi, G. Giunchi, M.E. Ruiz-Vizcaya, J. Chem. Phys. 68 (1978) 2337.
[77] D.R. Armstrong, P.G. Perkins, J.J.P. Stewart, J. Chem. Soc., Dalton Trans. (1972) 1972.
[78] K. Vanka, Z. Xu, M. Seth, T. Ziegler, Top. Catal. 34 (2005) 143.
[79] K. Vanka, Z.T. Xu, T. Ziegler, Organometallics 24 (2005) 419.
[80] S.H. Yang, J. Huh, W.H. Jo, Macromolecules 38 (2005) 1402.
[81] E. Zurek, T. Ziegler, Prog. Polym. Sci. 29 (2004) 107.
[82] Z.T. Xu, K. Vanka, T. Ziegler, Macromol. Symp. 206 (2004) 457.
[83] K. Vanka, Z.T. Xu, T. Ziegler, Macromol. Symp. 213 (2004) 275.
[84] P.G. Belelli, M.M. Branda, N.J. Castellani, J. Mol. Catal. A-Chem. 192 (2003) 9.
[85] Z.T. Xu, K. Vanka, T. Firman, A. Michalak, E. Zurek, C.B. Zhu, T. Ziegler, Organometallics 21 (2002) 2444.
[86] I.I. Zakharov, V.A. Zakharov, Macromol. Theor. Simul. 11 (2002) 352.
[87] G. Lanza, I.L. Fragala, T.J. Marks, Organometallics 21 (2002) 5594.
[88] E. Zurek, T. Ziegler, Organometallics 21 (2002) 83.
[89] F. Schaper, A. Geyer, H.H. Brintzinger, Organometallics 21 (2002) 473.
[90] K. Vanka, T. Ziegler, Organometallics 20 (2001) 905.
[91] E. Zurek, T. Ziegler, Inorg. Chem. 40 (2001) 3279.
[92] I.E. Nifant'ev, L.Y. Ustynyuk, D.N. Laikov, Organometallics 20 (2001) 5375.
[93] G. Lanza, I.L. Fragala, T.J. Marks, J. Am. Chem. Soc. 122 (2000) 12764.
[94] K. Vanka, M.S.W. Chan, C.C. Pye, T. Ziegler, Organometallics 19 (2000) 1841.
[95] S. Lieber, M.H. Prosenc, H.H. Brintzinger, Organometallics 19 (2000) 377.
[96] D. Braga, F. Grepioni, E. Tedesco, M.J. Calhorda, Z. Anorg. Allg. Chem. 626 (2000) 462.
[97] M.S.W. Chan, K. Vanka, C.C. Pye, T. Ziegler, Organometallics 18 (1999) 4624.
[98] V.A. Zakharov, E.P. Talsi, I.I. Zakharov, D.E. Babushkin, N.V. Semikolenova, Kinet. Catal. 40 (1999) 836.
[99] S. Beck, M.H. Prosenc, H.H. Brintzinger, J. Mol. Catal. A-Chem. 128 (1998) 41.
[100] R. Fusco, L. Longo, A. Proto, F. Masi, F. Garbassi, Macromol. Rapid Commun. 19 (1998) 257.
[101] R. Fusco, L. Longo, F. Masi, F. Garbassi, Macromolecules 30 (1997) 7673.
[102] R. Fusco, L. Longo, F. Masi, F. Garbassi, Macromol. Rapid Commun. 18 (1997) 433.
[103] M.J. Frisch, G.W. Trucks, H.B. Schlegel, G.E. Scuseria, M.A. Robb, J.R. Cheeseman, V.G. Zakrzewski, J.A. Montgomery Jr.,

R.E. Stratmann, J.C. Burant, S. Dapprich, J.M. Millam, A.D. Daniels, K.N. Kudin, M.C. Strain, O. Farkas, J. Tomasi, V. Barone, M. Cossi, R. Cammi, B. Mennucci, C. Pomelli, C. Adamo, S. Clifford, J. Ochterski, G.A. Petersson, P.Y. Ayala, Q. Cui, K. Morokuma, D.K. Malick, A.D. Rabuck, K. Raghavachari, J.B. Foresman, J. Cioslowski, J.V. Ortiz, A.G. Baboul, B.B. Stefanov, G. Liu, A. Liashenko, P. Piskorz, I. Komaromi, R. Gomperts, R.L. Martin, D.J. Fox, T. Keith, M.A. Al-Laham, C.Y. Peng, A. Nanayakkara, C. Gonzalez, M. Challacombe, P.M.W. Gill, B. Johnson, W. Chen, M.W. Wong, J.L. Andres, C. Gonzalez, M. Head-Gordon, E.S. Replogle, J.A. Pople, GAUSSIAN 98, Revision A.7., Gaussian Inc., Pittsburgh, PA, 1998.

[104] S.H. Vosko, L. Wilk, M. Nusair, Can. J. Phys. 58 (1980) 1200.

[105] A.D. Becke, Phys. Rev. A 38 (1988) 3098.

[106] J.P. Perdew, Y. Wang, Phys. Rev. B 45 (1992) 13244.

[107] V.R. Jensen, K.J. Børve, J. Comput. Chem. 19 (1998) 947.

[108] C. Gonzalez, H.B. Schlegel, J. Chem. Phys. 90 (1989) 2154.

[109] C. Gonzalez, H.B. Schlegel, J. Phys. Chem. 94 (1990) 5523.

[110] P.J. Hay, W.R. Wadt, J. Chem. Phys. 82 (1985) 284.

[111] P.J. Hay, W.R. Wadt, J. Chem. Phys. 82 (1985) 299.

[112] T.H. Dunning Jr., PJ. Hay, in: H.F. SchaeferIII (Ed.), Methods of Electronic Structure Theory, Plenum Press, New York, 1977, p. 1.

[113] R. Ahlrichs, M. Bär, M. Häser, H. Horn, C. Kölmel, Chem. Phys. Lett. 162 (1989) 165.

[114] J.P. Perdew, Phys. Rev. B 34 (1986) 7406.

[115] J.P. Perdew, Phys. Rev. B 33 (1986) 8822.

[116] K. Eichkorn, F. Weigend, O. Treutler, R. Ahlrichs, Theor. Chem. Acc. 97 (1997) 119.

[117] K. Eichkorn, O. Treutler, H. Ohm, M. Häser, R. Ahlrichs, Chem. Phys. Lett. 242 (1995) 652.

[118] K. Eichkorn, O. Treutler, H. Ohm, M. Häser, R. Ahlrichs, Chem. Phys. Lett. 240 (1995) 283.

[119] A. Klamt, G. Schuurmann, Perkin Trans. 2 (1993) 799.

[120] A. Schäfer, A. Klamt, D. Sattel, J.C.W. Lohrenz, F. Eckert, Phys. Chem. Chem. Phys. 2 (2000) 2187.

[121] P. Sherwood, A.H. de Vries, M.F. Guest, G. Schreckenbach, C.R.A. Catlow, S.A. French, A.A. Sokol, S.T. Bromley, W. Thiel, A.J. Turner, S. Billeter, F. Terstegen, S. Thiel, J. Kendrick, S.C. Rogers, J. Casci, M. Watson, F. King, E. Karlsen, M. Sjøvoll, A. Fahmi, A. Schäfer, C. Lennartz, J. Mol. Struct. (Theochem) 632 (2003) 1.

[122] S.R. Billeter, A.J. Turner, W. Thiel, Phys. Chem. Chem. Phys. 2 (2000) 2177.

[123] J.C.W. Lohrenz, T.K. Woo, T. Ziegler, J. Am. Chem. Soc. 117 (1995) 12793.